

Check for updates

From Snapshot to Movie: Visualizing Native Silk Spinning Defines the Paradigm for Bio-Inspired Spinning

Qinrui Lin, Yi Liu, Yumo Li, Liujingzhou Li, Fritz Vollrath, Minbiao Ji,* and Zhengzhong Shao*

Biomimetic spinning mimics natural filament formation by inducing stress-driven fibrillation of protein molecules into nano-filament bundles. Silk proteins, like fibroin or spidroin, have inspired analogues such as liquid crystals or micelles for spinning feedstocks. However, these often miss the dynamic nature of natural feedstocks, making stress-induced fibrillation difficult to replicate. A "flow-induced dehydration" hypothesis is proposed to explain how native silk proteins respond to stress during spinning. In Bombyx mori, fibroins transition from a homogeneous state in the posterior region to a two-phase structure in the middle gland. Dense entangled fibroins support conformational changes, while diluted regions ensure flowability. this model is validated using reconstituted silk feedstocks with induced phase separation, producing fibres with excellent mechanical properties and offering a new direction for bio-inspired fiber processing.

1. Introduction

The pull-trusion spinning of natural silks, be it in spiders or silkworms, is emerging as a model and paradigm for the production of fibers with a wide range of mechanical properties. [1] Importantly, the spinning technologies resembling the whole process of natural spinning, defined as biomimetic spinning, have been shown to be surprisingly cheap

Q. Lin, Y. Liu, L. Li, Z. Shao State Key Laboratory of Molecular Engineering of Polymers

Lab of Advanced Materials

Department of Macromolecular science

Fudan University

No. 2005 Songhu Road, Shanghai 200438, China

E-mail: zzshao@fudan.edu.cn

Y. Li, M. Ji

State Key Laboratory of Surface Physics and Department of Physics Key Laboratory of Micro and Nano Photonic Structures (Ministry of Education)

Shanghai Key Laboratory of Metasurfaces for Light Manipulation Fudan University

No. 2005 Songhu Road, Shanghai 200438, China

E-mail: minbiaoj@fudan.edu.cn

F. Vollrath

Department of Biology University of Oxford

South Parks Road, Oxford, Oxfordshire OX13RB, UK

(D)

The ORCID identification number(s) for the author(s) of this article can be found under https://doi.org/10.1002/adfm.202511413

DOI: 10.1002/adfm.202511413

energetically.[1a,2]Key for both, the costs of spinning and the mechanical properties of threads, seems to be the feature of stress-induced fibrillation.[3] Spider (arachnids) and silkworms (insects) have independently evolved silk spinning that in both cases relies on the formation of highly aligned microstructures. Existing spinning technologies that capture some specific features of natural spinning are defined as bio-inspired spinning. Such bio-inspired spinning technology focuses on promoting the mechanical performances of natural silks by aiming to copy their highly aligned microstructures rather than aiming to copy their economical process of stressinduced fibrillation. Typically, the processing of these bio-inspired feedstocks into filaments is achieved by non-biological

input of energy and/or chemicals reminiscent of the requirements associated with the production of synthetic fibers.^[4] In short, truly bio-mimetic spinning has so far eluded industry or indeed even laboratory benchmark trials

Biological stress-induced fibrillation can, in essence, be interpreted by two competing concepts assigning the assembly of native fibroins to analogues of either i) a type of liquid crystal or ii) an agglomeration of micelles.^[5] The fundamental gap between a) native fibroins of the natural feedstocks and b) reconstituted silk fibroins of the bio-inspired feedstocks is often attributed to structural differences: native Bombyx silk fibroins consist of both heavy and light chains, while reconstituted fibroins are mostly composed of heavy chains. This has led to the belief that truly biomimetic spinning can only be achieved by fully replicating the complex structures of native fibroins and closely mimicking the chemical environment of natural feedstocks.^[6] However, our findings outlined below demonstrate that stressinduced fibrillation is determined by specific molecular features and can be successfully replicated using regenerated fibroins, without the need to strictly replicate the natural feedstock composition.

Since stress-induced fibrillation is a dynamic transition, we must assume that the spinning process relies on how the organization of natural feedstocks evolves under the flow stress, rather than some specific and intermediate states identified as analogues of micelles or liquid crystallites. We assert that most modeling approaches largely ignore the fluidic properties of natural feedstocks during stress-

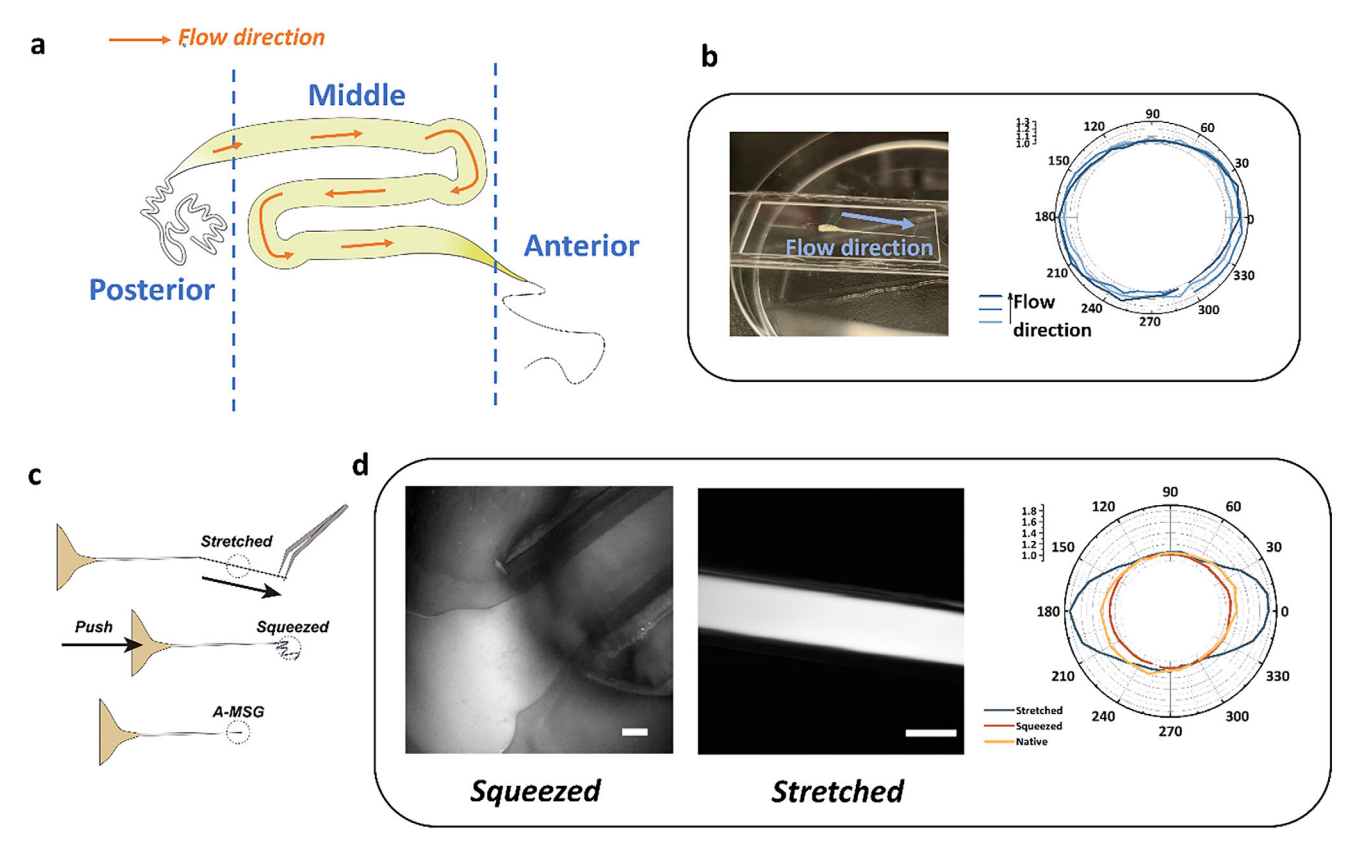


Figure 1. Dynamic transition processes in the anterior region of the silk gland (ASG) during biospinning. a) Schematic illustration of a silk gland of Bombyx Mori. A photograph of a dissected silk gland is in Figure S2 (Supporting Information). b) Left: photographs of a dissected ASG. Right: Characterizations of the microscale alignment by Stimulated Raman spectroscopy (SRS). Polarization dependence of the amide III band intensity of native fibroins inside the ASG. The amide I band is attributed to the C=O stretching of peptide bonds and can be used to characterize the alignment of protein chains. Compared to conventional Raman spectroscopy, the Raman signals in stimulated Raman scattering (SRS) are enhanced by $\approx 10^6$ to 10^7 times.^[9] This advantage enables SRS to monitor changes in the molecular structure of native fibroins in the ASG in real time.^[10] c) Schematic illustration of applying different flow-induced stresses to the native fibroins inside the ASG. The extensional stress is applied by stretching the native fibroins in the head of ASG. The compressive stress is applied by squeezing the back of the ASG. d) Left: SRS images of the native fibroins in ASG underwent different stresses. The Raman signals in these SRS images originate from the C-H vibration. Right: Polarization dependence of amide III band intensity of native fibroins underwent different stresses.

induced fibrillation.^[5b,7] In consequence, molecular-level guidance for preparing bio-inspired feedstocks tends to be missing.

Here, we apply the lens of the fluidic properties of natural feedstocks in order to examine the importance of hypothetical liquid crystalline and micelle morphology features. Appropriate fluidic properties comprise i) states of hydration as well as ii) responses to shear under a range of different flow scenarios. Our approach allows us to define and test hypothesis of the molecular behavior of natural feedstocks under conditions of spin extrusion. Accordingly, bio-inspired silk feedstocks were constructed for "artificial" spinning. The quality of our feedstocks was evaluated by characterization of i) their hydration states and ii) their responses to different flow conditions. The fibrillation processes were monitored through the stress-strain behaviors for assessing the biomimicry of our feedstocks during flow. The mechanical characteristics of the resulting fibers were compared with both natural silks and other so-called bio-inspired fibers.

2. Results and Discussion

2.1. Dynamic Transition in the Formation of the "Liquid Crystalline" State

Previous research identified the liquid crystalline state of native fibroins due to increased birefringence in the anterior region of the silk gland treated with chemical fixation. [8] This phenomenon is typically associated with fluids of highly aligned microstructures, such as liquid crystallites. Here we demonstrate that such aligned microstructures are formed by extensional flow and cannot be maintained in a static state. The microscale alignment of native fibroins in the anterior region of the silk gland was monitored by stimulated Raman spectroscopy (SRS) without involving any chemical treatment (Figure 1a,b; Figure S1, Supporting Information). In the static state, the native fibroins in natural feedstocks show isotropic Raman scattering intensity at various angles in the polarized plot of Raman spectra (Figure 1b), indicating minimal alignment. In the dynamic states, only the native

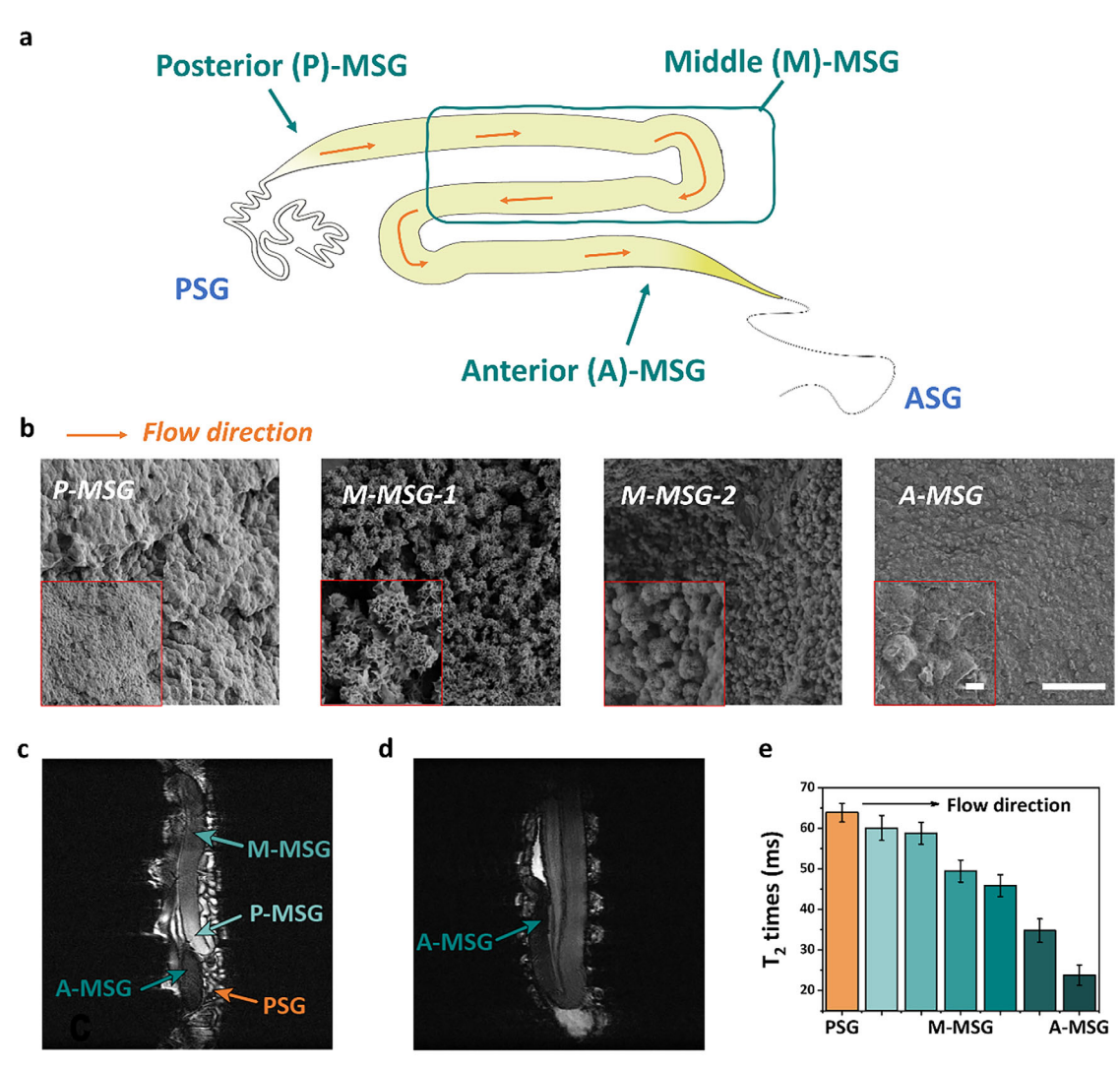


Figure 2. Dynamic transition processes in MSG during natural spinning. a) Schematic illustration of the different sections of MSG. b) Scanning electron microscopy (SEM) images of MSG in a fixed silk gland. All samples for SEM experiments were dehydrated by a critical point dryer and fractured in liquid nitrogen. Scale bars: 20 μ m for main images; insets 1 μ m. c) and d) T₂ MRI images of silkworms at sagittal and coronal views, respectively. e) The variation of T₂ relaxation times of natural feedstocks. Data were presented as mean±SD, n = 4 ROIs.

fibroins subjected to extensional flow exhibit anisotropic intensity in the polarized plot of Raman spectra (Figure 1c,d). The native fibroins under compressive flow remain isotropic and swell out of the gland (Figure 1d). These different responses to flows of native fibroins in the anterior region of the silk gland reveal that the increased birefringence of native fibroins is more likely to be caused by flow-induced orientation rather than any inherent properties, such as liquid crystallinity.

2.2. Dynamic Transition in the Formation of "Micellar" or "Liquid-Liquid Phase Separation" States

The micellar or liquid–liquid phase separation state was identified based on the globular morphology of native fibroins in the middle region of the silk gland (MSG).^[5b] It should be noted that such morphological features continuously change throughout

the MSG (Figure 2a). According to the changes, we divided the natural spinning process in MSG into three stages (Figure 2b). i) When homogenous natural feedstocks in the posterior region of the silk gland (PSG) enter the MSG (Figure S3, Supporting Information), native fibroins form interconnected spheres with rough surfaces; ii) In the middle of MSG, the spherical native fibroins transform into phase-separated structures with porous surfaces. The pore size of these spheres decreases along the flow direction during spinning (Figure S4a-c, Supporting Information). iii) In the tapered junction between MSG and ASG, the porous spheres begin to coalesce, and the porous surface diminishes (Figure S4d, Supporting Information). The three stages of changed morphology reveal that the underlying chain conformation is changed during natural spinning. This issue has been overlooked by simply generalizing native fibroins in natural feedstocks as analogues of micelles or liquid-liquid phase separation.

www.afm-journal.de

To directly visualize the dynamic changes of natural feedstocks in spinning, magnetic resonance imaging (MRI) was performed on an anesthetized vet spinning silkworm. T2-MRI images capture the hydration states of native fibroins in natural feedstocks by measuring the relaxation times of spin-spin interactions in water protons. [11] Increased hydration and fluidity generate bright T₂ MRI signals, ascribed to elevated water mobilities with prolonged T₂ relaxation times.^[12] The T₂-MRI contrast progressively darkens in spinning (Figure 2c,d; Figure S5, Supporting Information), revealing that this stage of natural spinning in the MSG is a continuous process of dehydration. By characterizing the secondary structures of native fibroins with different fluidities by Raman spectroscopy, we determined that dehydration is associated with increased aggregation of fibroin chains. This chain aggregation restricts the mobility of amide bonds, resulting in narrower peak width and higher relative intensity of the C=O stretching vibration (≈1660 cm⁻¹) compared to the aromatic rings (≈1616 cm⁻¹) (Figure S6, Supporting Information).^[13]

Besides the qualitative assessment of the dehydration in natural spinning, changes in T₂ relaxation times highlight two significant stages of dehydration and reduction of fluidity. The first occurs at the interconnection between PSG and MSG, where the T_2 relaxation time drops from 63.9 to \approx 58.1 ms (Figure 2e). This process is associated with the formation of phase separation, suggesting changes in underlying molecular structures in the metastable native fibroins. The second stage is at the tapered junction between MSG and ASG, where extensional stress is introduced, and the T2 relaxation times of natural feedstocks rapidly decrease from 49.5 to 23.8 ms (Figure 2e). This rapid dehydration reveals the critical role of extensional stress in natural spinning. Collectively, these results reveal the empirical implications of perceived interpretations of natural spinning by treating the observed intermediate state as a static equilibrium, while overlooking the dynamic changes occurring in the native fibroins of natural feedstocks. As a consequence, the bio-inspired feedstocks, as analogues of micelles or liquid crystals, require extra consumption of energy and chemicals for fibrillation.

2.3. Correspondences between Rheological Behaviors and Chain Conformations

However, current evidence is still insufficient to fully explain the dynamic changes of fibroin chains during stress-induced fibrillation. To investigate these changes at the molecular level, we applied different types of flow stress to natural feedstocks and examined their molecular behaviors through rheological parameters. In natural spinning, two types of flow-induced stresses are applied to natural feedstocks: shear and extensional stress. Extensional stress arises from elongational flow deformation, which results from the tapered dies used in biospinning.^[14] During elongational flow, the fibroin chains are stretched, generating internal stress that resists deformation through interchain interactions. Extensional viscosity measures this resistance to flow. In this study, we developed an apparatus for uniaxial stretching to measure extensional viscosity while minimizing shear stress integration (Figure S7, Supporting Information), because uniaxial stretching of solutions only integrates elongation deformation rather than internal frictions between flow layers.[14a,15] For all natural feedstocks from different sections of the glands, extensional viscosity increases as deformation (measured as strain) increases (**Figure 3a**,b; Figure S8, Supporting Information). This strain-hardening behavior is typically attributed to interchain associations, which act like "hooks" that resist deformation. Since native fibroins have linear structures and show negligible conformation transitions, as observed in the Raman spectra (Figure S9, Supporting Information), the strain-hardening properties are likely due to entanglements, [14a] like those in linear polymers.

It is important to note that the extensional viscosity of natural feedstocks decreases at higher extensional rates. This is uncommon for conventional polymers. [16] Similar behaviors have been observed in wormlike micelle solutions with two-phase structures, where the micelle's inner region exhibits solid-like rheological behavior, while the interspaces behave like liquids. [17] Based on this analogy, we propose that the inner and interspaces of globular native fibroins contribute separately to both the strainhardening behavior and the thinning behavior at higher extensional rates. The strain-hardening is assigned to the entangled inner space of the globular fibroins, which promotes fibroin dehydration (Figure 3c). In contrast, the thinning behavior results from the disentangled interspace, which facilitates the extensibility of natural feedstocks.

Next, we examined how natural feedstocks respond to shear flow. Shear force arises from friction between fluid layers [14a], which can disentangle fibroin chains (Figure 3d). The main effect of shear stress is a transition in the secondary structure, which is prevented by entanglement. According to the amide I band (ranging from 1200-1350 cm⁻¹) in the Raman spectra (Figure 3e; Figure S10, Supporting Information), native fibroins have an amide I band centered at 1260 cm⁻¹, indicating random coil structures. [18] After applying shear stress, the amide I band the amide I band shifts to 1240 cm⁻¹, indicating the formation of regularly folded β -sheets. This type of secondary structure transition under shear stress has not been observed in homogeneous regenerated solutions.^[19] Since natural feedstocks possess hydrogel-like properties, we interpret the shear-induced β-sheet formation as analogous to the shear-induced crystallization of polymer melts. Both processes rely on the critical role of metastable phase separation, which aids crystallization by promoting conformational ordering and segment orientation.[20-21]

Molecular behaviors under shear stress were analyzed by examining changes in rheological parameters, specifically the elastic and viscous responses. Elastic responses, which describe the material's ability to store energy, were measured by the storage modulus. Viscous responses, which describe the material's ability to dissipate energy, were measured by the loss modulus. We first assessed the relative contributions of these two parameters in relation to the degree of deformation. Natural feedstocks from the middle section of MSG exhibit an elastic-dominated range up to ≈20% strain, whereas those from the posterior and anterior sections of MSG exhibit elastic-dominated behavior up to ≈100% strain (Figure 3f). The shorter elastic-dominated range in M-MSG feedstocks suggests they are more prone to disentanglement compared to the other sections. This may be linked to the morphological differences in interspace structures: The feedstocks from the posterior and anterior sections of MSG show interconnected morphologies, while the feedstocks from the middle are fully phase-separated.

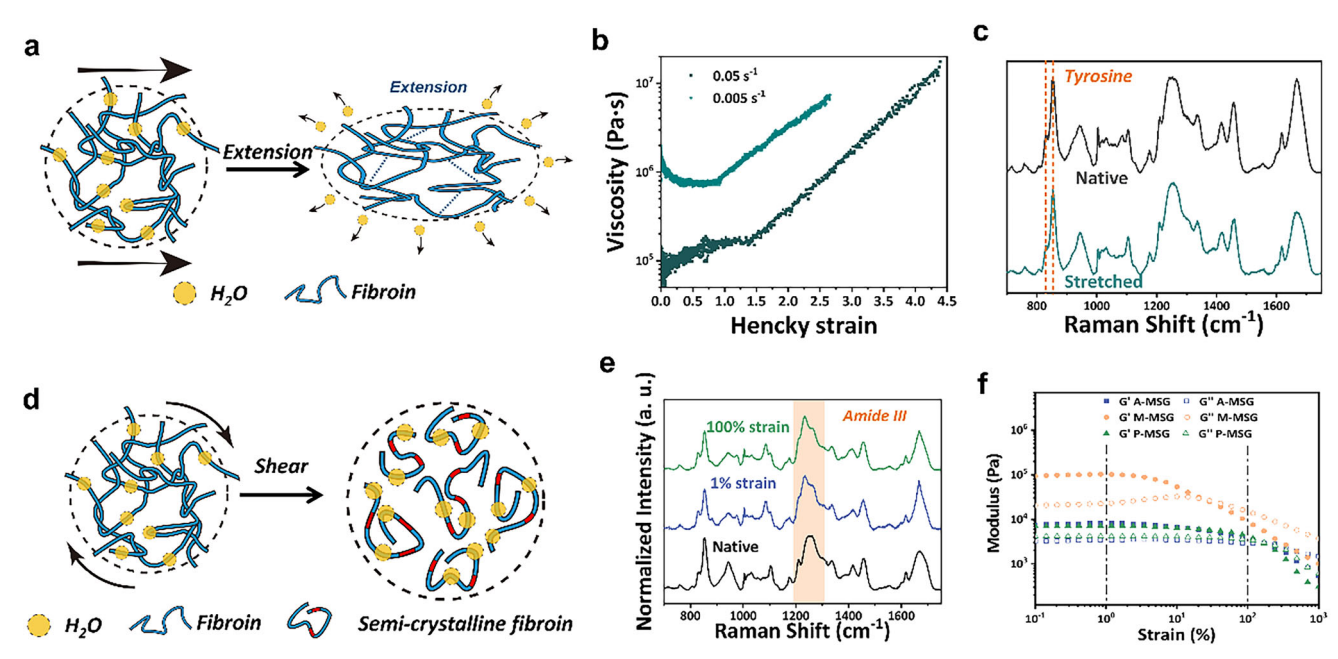


Figure 3. Correspondence between rheological behavior and chain conformation. a) Schematic illustration of the chain conformation of native fibroins under extensional stress. b) Transient extensional viscosity of natural feedstocks from the middle region of MSG plotted against Hencky strain (a measure of deformation). c) Raman spectra of native fibroins before and after stretching. The relative intensity of tyrosine bands (l_{850}/l_{830}) is 2.6 ± 0.1 for native fibroins and 2.9 ± 0.1 for stretched native fibroins. The increase of this value is attributed to the elevated level of hydrophobicity around tyrosine residues. For the stretched natural feedstocks, this phenomenon is related to expel hydration water as observed in the MRI images. d) Schematic illustration of the chain conformation of native fibroins under shear stress. e) Raman spectra of native fibroins extracted from M-MSG sheared at 1% and 100% strain. The spectra were acquired using a 785 nm laser with a grating density of 1800 gr mm⁻¹. f, The variations of storage (filled) and loss (hollow) modulus at different degrees of shear deformation (measured as strain).

We also monitored changes in viscoelasticity during β -sheet formation. Since β -sheets are regularly folded structures, they enhance the fibroin chains' ability to store energy, as reflected by the continuous increase in storage modulus across all natural feedstocks from different gland sections (Figure S12, Supporting Information). However, the loss modulus, which reflects energy dissipation, showed differences among the sections (Figure S12, Supporting Information). While the loss modulus in fibroins from the posterior and anterior sections of MSG remained stable under shear stress, the loss modulus of fibroins from the middle sections of MSG continued to increase. This behavior aligns with earlier observations that the feedstocks from the middle sections of MSG are more prone to disentanglement, which corresponds to weaker inter-fibroin associations.

2.4. Molecular Behaviors of the Flow-Induced Fibrillation Process

The molecular behavior under shear stress underscores the role of disentanglement in facilitating the deformation of highly concentrated native fibroins. Based on these observations, we propose that the key molecular requirement for the biospinning process is the presence of metastable two-phase structures (**Figure 4**). A dense phase formed by entangled fibroins undergoes dehydration due to extensional stress, promoting the formation of β -sheets under shear stress. Meanwhile, the interspace of these dense phases becomes disentangled, providing the extensibility needed for fibroin deformation. As a result, globular native fi-

broins can be easily transformed into elongated building blocks when entering the anterior section of the silk gland. The weakly associated interspaces enable these building blocks to form oriented structures in the ASG, which then serve as precursors to the highly oriented microstructures found in natural silk.

While our proposed hypothesis helps to integrate previously fragmented understandings of the biospinning process, it primarily focuses on native proteins within the middle silk gland. Direct and quantitative evidence of protein assembly in the anterior silk gland, posterior silk gland, and spinneret remains lacking due to the challenges in accessing and analyzing native feedstocks in these regions. Acquiring such data will require the development of precise, in situ characterization methods. Moreover, we have observed that the geometry of silk glands varies among species, such as in spiders and *Antheraea pernyi* (Chinese tussah silk). These anatomical differences may lead to variations in flow stress during spinning. Therefore, the general applicability of our flow-induced dehydration hypothesis should be further tested across different silk-spinning species.

2.5. Natural Feedstocks and Bio-Inspired Feedstocks

To validate our natural spinning hypothesis, we sought to mimic the stress-induced fibrillation process using reconstituted silk fibroin (RSF)-based feedstocks with similar phase separation structures. Phase separation in the RSF solutions was induced by adding phosphate ions, which shielded the interactions between

Figure 4. Schematic illustration of the biospinning process propounded in this research. The native fibroins in PSG (orange shaded) are in a homogeneous state. The native fibroins in MSG (cyan shaded) are in phase phase-separated state, which was recognized as analogues of micelles. The fibroin chains are initially interconnected and transformed into an entangled, separated state. The degree of entanglement is elevated along the flow direction. The spherical native fibroins are elongated in the tapered junction between MSG and ASG because of the integrated extensional stress. The native fibroins form elongated droplets in ASG (blue shaded) and undergo crystallization along the flow direction. The elongated fibroins were aligned by flow stress so that increased birefringence could be observed. The elongated droplets serve as the precursor of fibril bundles as the building blocks of hierarchically aligned natural silks (Figure S12, Supporting Information).

RSF chains (Figure 5a). The phase-separated RSF solutions (RSF-LLPS) consist of two liquid phases: micro-sized droplets forming the dense phase, and the remaining solution constituting the dilute phase. Also, we noticed the required amounts of phosphate ions increased in acidic RSF solutions. Since RSF becomes less charged in low-pH environments, the mechanism for phosphate ions inducing phase separation is reducing electrostatic repulsion and necessitating higher ionic strength to trigger phase separation. These findings support the hypothesis that phosphate ions promote LLPS mainly by weakening interchain electrostatic interactions.

It should be noted that the LLPS solutions were formed using $\approx \! 3$ wt.% RSF because it corresponds to the initial concentration obtained after dissolving degummed silk in LiBr, without further concentration. Although both lower and higher concentrations can form LLPS, each presents specific challenges. Lower concentrations require less phosphate due to weaker interchain associations, but they lack sufficient viscosity for pre-fiber formation and are less cost-efficient. Higher concentrations, on the other hand, require significantly more phosphate to induce LLPS and are prone to precipitation due to salt overload in the dense phase.

Before studying the dynamic properties, we analyzed the differences between native and reconstituted fibroin in homogeneous solutions. Native fibroins consist of both heavy and light chains. While reconstituted fibroins are degraded and primarily composed of heavy chains.^[22] With the same mass concentrations, the presence of the hydrophilic light chain in native fibroins allows them to form phase-separated solutions at a lower

concentration of phosphate ions compared to reconstituted fibroins (Figure S13, Supporting Information). We hypothesized that stronger interchain interactions between heavy chains in regenerated fibroins require a higher concentration of phosphate ions to effectively shield these interactions.

To support this hypothesis, we compared the changes in water mobility between phase-separated RSF and homogeneous RSF solutions at the same concentrations. Notably, water mobility in homogeneous RSF solutions was more restricted compared to RSF-LLPS solutions (Figure 5b). Conversely, for native fibroins, water mobility in the homogeneous PSG region was higher than in the phase-separated solutions. Such a difference highlights the importance of hydrophilic light chains for stabilizing native feed-stocks at high concentrations. While RSF, without light chains to segregate heavy chains, possesses strong interchain interactions, which act as an energy barrier to fibrillation. In other words, focusing heavily on increasing feedstock concentration may produce unintended side effects in bio-inspired spinning processes.

2.6. The Responses of Bio-Inspired Feedstocks to External Flow

To investigate the flow-sensitive properties of the dense phase, we compared changes in chain conformation and hydration states before and after applying external stress. It should be noted that the concentration of the dense phase, obtained via gravity settlement or centrifugation, was ≈ 8 wt.%, providing an ideal viscosity for pre-fiber formation. The dense phase subjected to

16163028, 0, Downloaded from https://advanced.onlinelibrary.wiley.com/doi/10.1002/adfm.202511413 by Fudan University, Wiley Online Library on [26/09/2025]. See the Terms and Conditions (https://onlinelibrary.wiley.com/term

and-conditions) on Wiley Online Library for rules of use; OA articles are governed by the applicable Creative Commons License

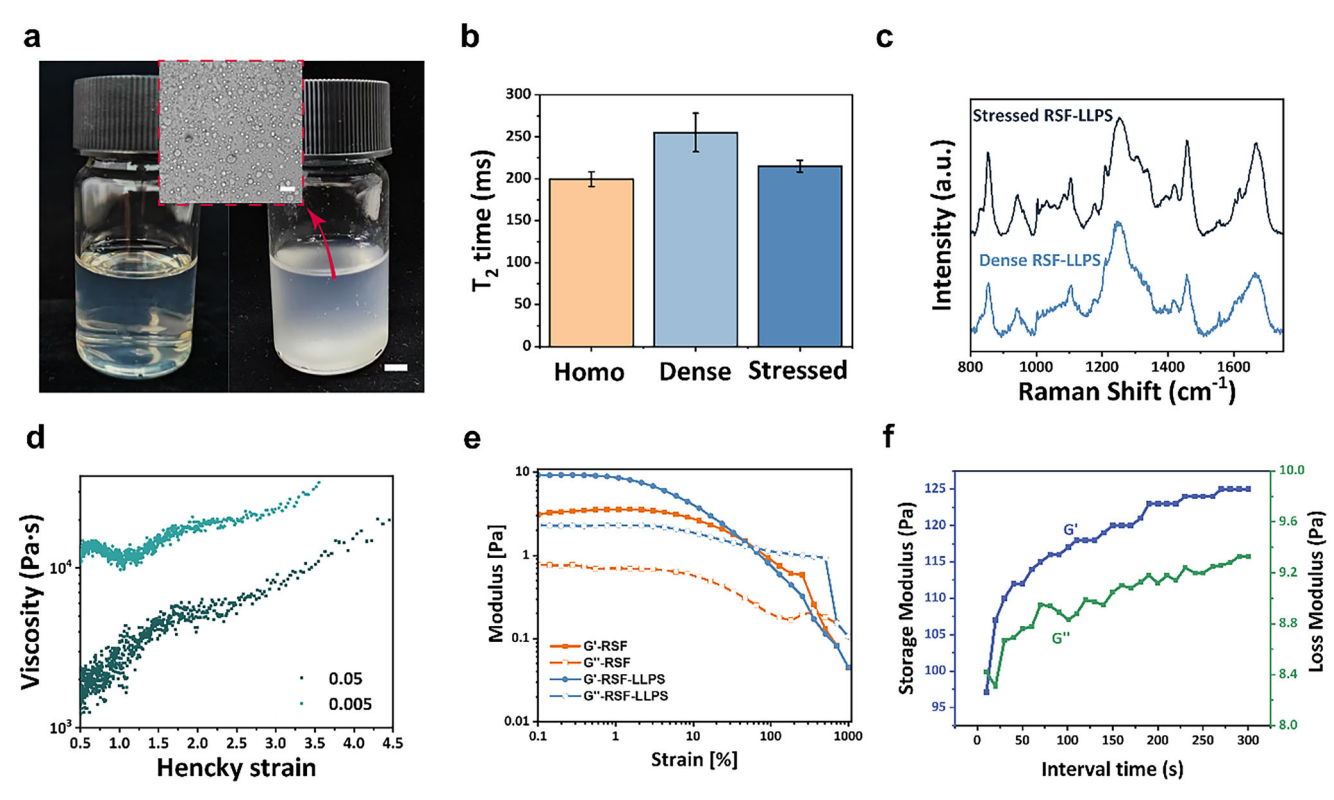


Figure 5. Dynamics and Properties of LLPS in Regenerated Silk Fibroin Systems. a) Photographs of RSF solution (left), RSF-LLPS solution (right), and a microscope image showing micro-sized droplets within RSF-LLPS (inset). Scale bar: $500 \, \mu m$. b) T_2 relaxation times of homogenous RSF solutions (Homo), dense phase of RSF-LLPS (Dense), and stressed RSF-LLPS (Stressed). Data were presented as mean±SD, $n = 4 \, \text{ROIs.}$ c) Raman spectra of the dense phase of RSF-LLPS, separated by centrifugation (Stressed) and gravity settlement (Dense). The spectra were acquired using a 785 nm laser with 1800 gr mm⁻¹ grating density and 3 s accumulation. d) Transient extensional rheology of stressed RSF-LLPS feedstocks with two different extensional rates. e) Variation of storage/loss modulus of stressed RSF-LLPS feedstocks at different degrees of deformation. f) Variation of storage and loss modulus of stressed RSF-LLPS feedstocks in oscillation shear rheology tests with 1% and 100% strain.

external stress exhibited shortened T_2 relaxation times (Figure 5b), indicating dehydration. Along with dehydration, changes in the amide I Raman band—such as a narrowed peak width and increased relative intensity—suggest that dehydration enhances chain aggregation (Figure 5c). These changes in T_2 relaxation times and the amide I Raman band are consistent with results obtained from natural feedstocks, corroborating that both natural and our bio-inspired feedstocks share similar flow sensitivity.

Next, we examined the responses of the dense phase in RSF-LLPS to extensional and shear flow. Under extensional stress, RSF-LLPS exhibited biomimetic strain-hardening at a fixed extensional rate, and thinning behavior as the extensional rate increased (Figure 5d). Additionally, the dehydration process under extensional stress was directly observed (Figure S14 and Video S1, Supporting Information).

In shear rheology, the storage moduli of both RSF-LLPS and stressed RSF-LLPS solutions showed thickening behavior at 1% strain, similar to natural feedstocks (Figure 5e,f). The loss modulus remained nearly stable, akin to the connected structures in natural feedstocks (Figure 5f). These findings confirm that the phase-separated droplets are associated with weak physical interactions, similar to those seen in natural feedstocks. Since these responsive properties to external stress were not observed in con-

centrated homogeneous RSF solutions (Figure S15, Supporting Information), we can conclude that the molecular architecture formed through phase separation is essential for the dynamic properties of both native and regenerated fibroins.

2.7. Bio-Inspired Spinning Using Artificial Phase-Separated Feedstocks

Encouraged by the shared dynamic properties between natural and our bio-inspired feedstocks, we tested their ability to undergo stress-induced fibrillation and monitored changes in their microstructures during this process (**Figure 6a**). Upon stretching, the viscous RSF-LLPS feedstocks initially form fibers with highly aligned building blocks, without the formation of β -sheets (Figure 6b; Figure S16, Supporting Information). These fibers can be significantly extended through additional stretching, during which β -sheets are formed.

Based on changes in the force-strain curves during this process, bio-inspired fibrillation can be divided into two stages (Figure 6c): 1) Initial fiber formation stage: Characterized by a broad yielding plateau, where the stress is primarily generated by the elongation of globular dense phases. 2) β -sheet formation stage: Marked by the coexistence of a yield point and a

www.afm-journal.de

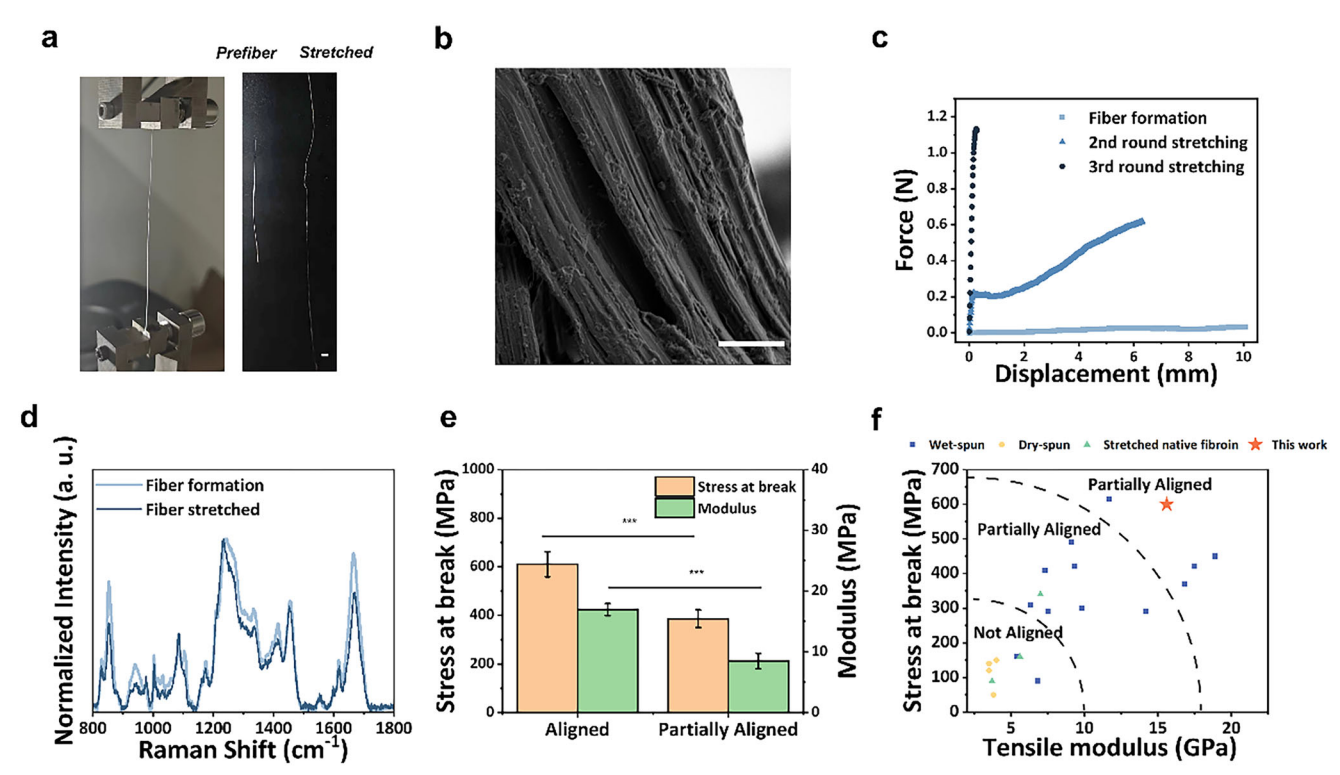


Figure 6. Structure and Mechanical Properties of our bio-inspired fibers. a) Left: Photographs of the fibrillation process. Right: pre-fiber formed from stretching the stressed RSF-LLPS feedstocks and the stretched pre-fiber. Scale bar is $100 \, \mu m$. b) Scanning electron microscopy (SEM) images of stretched prefiber. Scale bar: $10 \, \mu m$. c) Force-displacement of the prefibers in the repeated stretching process. d) Raman spectra of the prefiber and the stretched prefiber, acquired using a 785 nm laser with $1800 \, \text{gr/mm}$ grating density and an accumulation time of 3s. e) Stress at break and modulus of aligned and partially aligned bio-inspired fibers. Data presented as mean \pm SD, n = 10, statistical significance, $^{***}p \leq 0.001$. f) The ultimate strength and stiffness of our biomimetic fibers versus existing artificial fibers produced by conventional bio-inspired spinning methods. [1a,23]

hardening region, where the friction between elongated building blocks generates shear forces, promoting β -sheet formation and further alignment (Figure 6d). Both stages contribute to increasing the force. The disentangling of the building blocks ensures that the regenerated fibroins are fully aligned during repeated stretching, reducing yielding behavior after successive stretches. These two stages of fibrillation closely replicate the natural spinning process seen in A-MSG and ASG, without the need for harsh experimental conditions.

The obtained fiber still demonstrates brittle features because of large amounts of phosphate ions and incomplete β -sheet formation. The finalization of bio-inspired fibers requires salt removal and crystallization in a 30% ethanol solution. To our surprise, the fibers displayed coloration under polarized light, which is correlated to highly ordered internal structures, enabling them to act as diffraction gratings (Figure S17, Supporting Information). The mechanical performances of our bio-inspired fibers are closely linked to their microscopic alignment. Highly aligned fibers exhibit a remarkable ultimate strength of 610 ± 51 MPa and stiffness of 17.0 \pm 1.0 GPa (n = 10) (Figure 6e; Figure S18, Supporting Information). The standard deviation of these data comes from the defects and inhomogeneity in fiber formation. In contrast, partially aligned fibers—those produced without repeated stretching during the bio-inspired spinning process—show reduced strength but increased toughness (Figure 6e; Figure S19a, Supporting Information). These findings confirm that crystallization and alignment improvement can be achieved simultaneously, as observed in the natural spinning process. The above data demonstrate our bioinspired spinning method can reduce both chemical usages, by avoiding large coagulation baths, and energy consumption, by eliminating high-energy sonication steps. These advantages highlight the potential of our LLPS-based approach for future scale-up. While this section primarily serves to validate the underlying mechanism rather than to propose an industrial production method, the practical efficiency of our bioinspired spinning in large-scale production remains to be estimated.

Moreover, the strength and stiffness of our fibers outperform most existing fibers created through perceived biospinning methods and native silkworm silks (Figure 6f; Figure S19b, Supporting Information). Such performances are lower than those of force-reeled native silks (Figure S19b, Supporting Information) and have the potential for further improvement by elaborating processing parameters. According to the structure-property relationship of semicrystalline polymer fibers, the stiffness and strength of our bio-inspired fibers are closely linked to the alignment of β -sheets. In our draw-spinning method, this alignment is influenced by several factors, including the stretching speed during both pre-fiber formation and post-stretching, as well as the maintenance of internal stress during ethanol treatment. Notably, the solvent exchange process during ethanol treatment may introduce inhomogeneity between the outer and inner layers of

the fiber due to differential diffusion of water and ethanol. Therefore, optimizing this draw-spinning approach requires a detailed analysis of the crystallization kinetics and solvent exchange dynamics.

Beyond the processing parameters, the above fiber formation process demonstrates that RSF-LLPS solutions can replicate key features of stress-induced fibrillation observed in natural biospinning. However, it is important to note that in native silk spinning, pre-fiber formation, dehydration, and crystallization occur within the duct, where flow stress and the chemical environment are precisely and continuously regulated. Our bio-inspired fiber formation serves as a preliminary validation of the flow-based hypothesis, but does not fully replicate these tightly controlled conditions. The potential of RSF-LLPS feedstocks for biomimetic spinning can be further tested using microfluidic devices, which can better mimic the spatial and temporal regulation of the natural silk

3. Conclusion

In this study, we distinguish the process of natural spinning from the dynamic morphing of the native fibroin molecules. By identifying relationships between the dynamic properties and the morphological features of these fibroins, we outline a molecular framework contributing to how natural feedstocks respond to external stress for fibrillation. In natural feedstocks, native fibroins form entangled dense phases that undergo successive phases of extensional deformation, which aligns them into the building blocks fundamental for the formation of the fiber. These phaseseparated macromolecular structures, in their disentangled state, allow extensibility at very high concentrations. We propose that the essence of natural spinning lies in the flow-responsive properties of these phase-separated structures. We validate this concept by examining the convergence of dynamic properties between native fibroins and artificial LLPS solutions formed by phosphate ions. In other words, the observed dynamic transition can biomimetically be achieved by replicating chain conformations, without the need to precisely replicate the chemical environment of appropriate artificial feedstocks. Changes in chemical environments, such as pH levels and ion concentrations, facilitate the stress-induced fibrillation process but are not its primary cause. Using this framework, our set-up produced fibers with outstanding mechanical properties by allowing the formation of highly aligned microstructures similar to those found in the native model silk of Bombyx as well as other animal silks. Importantly for practical use, the consumption of both energy and chemicals was minimized in our biomimetic spinning process by eliminating multistep concentration and coagulation.

In summary, this study redefines our understanding of natural spinning and highlights the critical role of bio-inspired phase separation in polymer processing. The unique phase separation observed in the silk gland has important implications for the fabrication of synthetic polymers into highly ordered, mechanically strong fibers. By drawing insights from natural systems, this work not only deepens our knowledge of fiber formation but also paves the way for new innovations in synthetic fiber production.

4. Experimental Section

Preparation of Fixed Silk Glands: The silk glands, extracted from fifth instar Bombyx mori silkworms during silk spinning, were initially rinsed with 0.1 M PB buffer three times for 10 min each to remove sericin, followed by a 12 h immersion in modified Karnovsky fixative. This fixative comprised 2% glutaraldehyde, 2% formaldehyde, 0.1 м sodium cacodylate, 0.01 M calcium chloride, and 0.35 M sodium chloride, pH adjusted to 7.4 using hydrochloric acid. After fixation, the glands were further cleansed with 0.1 M PB buffer and deionized water to eliminate any residual salts.

Preparation of Silk Spinning Feedstocks: The silk spinning feedstocks were obtained from freshly dissected glands of fifth instar Bombyx mori silkworms. Initially, the silkworms were carefully dissected to remove their glands, which were then placed in a Petri dish. To remove the sericin, the glands were thoroughly washed with an isotonic 0.75 M NaCl solution. Using fine tweezers, the epithelium was delicately peeled off, and the gland contents were once again rinsed in the isotonic salt solution to ensure thorough cleansing.

Preparation of Regenerated Silk Fibroin LLPS Solution: The regenerated silk fibroin aqueous solution was prepared from Bombyx mori silkworm cocoons using a well-established procedure described previously. Initially, the cocoons were degummed by boiling them in a 0.5 wt.% NaHCO3 solution for 45 min. After a thorough rinse with deionized water and drying, the silk was then dissolved in a 9.3 mol L^{-1} LiBr solution at 60 °C for an hour. This solution underwent dialysis against deionized water for three days to totally remove the LiBr, resulting in a silk fibroin aqueous solution with a protein concentration of \approx 4 wt.%.

After dilution to a 3 wt.% concentration, the regenerated silk fibroin solution had 0.75 M phosphate buffer (pH = 7) added dropwise until reaching a final phosphate concentration of 0.125 M. This prepared solution was subsequently stored at 4 °C for 12 h, with intermittent shaking every 30 min during the initial 3 h, to ensure the formation of a stable LLPS solution. The dense phase of the prepared LLPS solution was subsequently separated either by natural sedimentation at room temperature or by centrifugation.

To ensure consistency in the properties of RSF-LLPS dense phases, the separation process was standardized by carefully controlling the mass and speed during centrifugation to maintain consistent centrifugation stress. For gravity settlement, the process was conducted at 4 °C to slow down phase separation and minimize external stress. Comparative tests show that both methods yield dense phases with comparable morphology and rheological behavior.

Fabrication of Biomimetic Silk via LLPS: To fabricate the protofibrils of biomimetic silk via LLPS, the dense phase obtained from silk LLPS through centrifugation was constantly stretched at a speed of 50 µm s⁻¹. This process utilized a Physica MCR 301 rheometer (Anton Paar GmbH, Austria) configured with an 8 mm parallel plate and a 1 mm gap distance. The protofibrils were first immersed in a 50% ethanol solution for 10 min and then, while still in the solution, gently stretched to twice their length using tweezers. After this process, they were allowed to dry and subsequently

Characterization: Surface and cross-sectional scanning electron microscopy (SEM) images were obtained by using a Zeiss Gemini SEM 500 at 3 kV. SRS measurements were performed using a custom-built SRS microscope. The SRS system employed a tunable pump beam and a fixed Stokes beam, generated by an OPO laser (Insight DS+, Newport, CA), with picosecond chirping for resolution. The beams, modulated for intensity, were merged and directed into a laser scanning microscope (FV 1200, Olympus) using a 60× water immersion objective lens. The transmission light was filtered, detected, and demodulated to acquire the simulated Raman loss (SRL) signal, enabling imaging. A motorized stage adjusted beam delays for rapid SRS image capture, simplifying the process of assembling and obtaining detailed images. All MRI images were acquired by using a 7.0 T Novila magnetic resonance imaging system (Chen-Guang Medical, China). A spinning silkworm was anesthetized with 1% isoflurane. T2-weighted images were acquired with a TR of 2000 ms, TE of 17.8 ms, and a 1 mm slice thickness. T2 relaxation times were measured using a multi-echo turbo spin-echo sequence (TR = 5500 ms, 0.8 mm

www.afm-journal.de

1616328, 0, Downloaded from https://advanced.onlinelibrary.wiley.com/doi/10.1002/adfm.202511413 by Fudad University, Wiley Online Library on [2609/2025]. See the Terms and Conditions (https://onlinelibrary.wiley.com/terms-and-conditions) on Wiley Online Library for rules of use; OA articles are governed by the applicable Creative Commons Licenses

slice thickness). Signal intensities were fitted to a mono-exponential decay model using prim software to generate T_2 maps. The T_2 relaxation times were obtained by randomly selecting 4 regions of interest on the T_2 map.

Shear rheological tests were conducted at 25 °C using a Physica MCR 301 rheometer (Anton Paar GmbH, Austria) in a strain-controlled mode with a 10 mm taper-plate configuration and a 0.4 mm gap. To prevent evaporation, a small amount of low viscosity mineral oil was applied at the edge of the dense phase. The constant strain oscillation experiments were performed at 1% and 100% strain levels for 300 s each. For extensional rheology tests, the setup was adjusted to an 8 mm parallel-plate with a 1 mm gap. The diameter of the protofibrils during extension was monitored using an optical microscope camera. The mechanical properties of biomimetic LLPS silk were tested on an Instron 5565 mechanical testing machine (Instron, Norwood, USA) with a load cell of 2.5 N. All tests were carried out at 20-25 °C and relative humidity of 50-60%. The cross-sectional area of each fiber was calculated by determining the diameter using an optical microscope and then multiplying it by the shape factor, which was statistically derived from analyses conducted with Field Emission Scanning Electron Microscopy (FESEM).

Statistical Analysis: The value of n=4 indicates the number of independently selected ROIs in the T_2 maps, and the data were presented as mean \pm SD.

Supporting Information

Supporting Information is available from the Wiley Online Library or from the author

Acknowledgements

Q. L. and Y. L. contributed to this work. This work was supported by the National Natural Science Foundation of China (No. 21935002 to Z. Shao). The authors declare no competing financial interest.

Conflict of Interest

The authors declare no conflict of interest.

Data Availability Statement

The data that support the findings of this study are available from the corresponding author upon reasonable request.

Keywords

 $biomimetic\ spinning,\ liquid-liquid\ phase\ separation,\ natural\ spinning$

Received: May 7, 2025 Revised: June 30, 2025 Published online:

a) A. Koeppel, N. Stehling, C. Rodenburg, C. Holland, Adv. Funct. Mater. 2021, 31, 2103295; b) A. D. Malay, T. Suzuki, T. Katashima, N. Kono, K. Arakawa, K. Numata, Sci. Adv. 2020, 6, abb6030.

- [2] a) F. Vollrath, D. Porter, *Polymer* 2009, 50, 5623; b) P. Mohammadi, A. S. Aranko, L. Lemetti, Z. Cenev, Q. Zhou, S. Virtanen, C. P. Landowski, M. Penttilä, W. J. Fischer, W. Wagermaier, *Comm. Biol.* 2018, 1, 86.
- [3] a) A. D. Malay, H. C. Craig, J. Chen, N. A. Oktaviani, K. Numata, Biomacromolecules 2022, 23, 1827; b) Z. Shao, F. Vollrath, Nature 2002, 418, 741; c) J. L. Yarger, B. R. Cherry, A. Van Der Vaart, Nat. Rev. Mater. 2018, 3, 1i8008.
- [4] a) Y. Liu, J. Ren, S. Ling, Compos. Commun. 2019, 13, 85; b) K. Yazawa, A. D. Malay, N. Ifuku, T. Ishii, H. Masunaga, T. Hikima, K. Numata, Biomacromolecules 2018, 19, 2227; c) S. Ling, Z. Qin, C. Li, W. Huang, D. L. Kaplan, M. J. Buehler, Nat. Commun. 2017, 8, 1387.
- [5] a) F. Vollrath, D. P. Knight, Nature 2001, 410, 541; b) H.-J. Jin, D.
 L. Kaplan, Nature 2003, 424, 1057; c) M. Landreh, H. Osterholz, G.
 Chen, S. D. Knight, A. Rising, A. Leppert, Commun. Chem. 2024, 7, 260
- [6] S. Yang, Y. Yu, S. Jo, Y. Lee, S. Son, K. H. Lee, Nat. Commun. 2024, 15, 10394.
- [7] a) D. Fedorov, F. E. Sammalisto, A. L. Harmat, M. Ahlberg, S. Koskela, M. P. Haataja, A. Scacchi, M. Sammalkorpi, M. B. Linder, Adv. Funct. Mater. 2025, 35, 2410421; b) A. D. Malay, N. A. Oktaviani, J. Chen, K. Numata, Adv. Funct. Mater. 2025, 35, 2408175.
- [8] T. Asakura, K. Umemura, Y. Nakazawa, H. Hirose, J. Higham, D. Knight, Biomacromolecules 2007, 8, 175.
- [9] a) L. Gong, S. Lin, Z. Huang, Laser Photonics Rev. 2021, 15, 2100069;
 b) B. Manifold, S. Men, R. Hu, D. Fu, Nat. Mach. Intell. 2021, 3, 306.
- a) Y. Li, B. Shen, S. Li, Y. Zhao, J. Qu, L. Liu, Adv. Biol. 2021, 5, 2000184;
 b) Q. Cheng, Y. Miao, J. Wild, W. Min, Y. Yang, Matter 2021, 4, 1460.
- [11] a) W. Zhao, Z. Lei, B. Wu, p. Wu, Angew. Chem., Int. Ed. 2024, 136, 202400531; b) Y. Shi, B. Wu, S. Sun, P. Wu, Adv. Mater. 2024, 36, 2310576.
- [12] a) A. Elias, A. Tsourkas, Nanotech. Hemat. 2009, 2009, 720; b) B. R. Smith, S. S. Gambhir, Chem. Rev. 2017, 117, 901.
- [13] a) M.-E. Rousseau, T. Lefèvre, L. Beaulieu, T. Asakura, M. Pézolet, Biomacromolecules 2004, 5, 2247; b) J. Dionne, T. Lefèvre, M. Auger, Int. J. Mol. Sci. 2016, 17, 1353.
- [14] a) F. N. Cogswell, Polymer melt rheology: A guide for industrial practice, Elsevier, Amsterdam, Netherlands, 1981; b) A. Koeppel, P. R. Laity, C. Holland, Soft Matter 2018, 14, 8838.
- [15] N. Kojic, J. Bico, C. Clasen, G. H. McKinley, J. Exp. Biol. 2006, 209, 4355.
- [16] H.-C. Tseng, Korea-Aust. Rheol. J. 2023, 35, 349.
- [17] a) E. Miller, C. Clasen, J. P. Rothstein, Rheol, Acta 2009, 48, 625; b) S. R. Raghavan, Y. Feng, Wormlike Micelles: Solutions, Gels, or Both?, (Eds. C. A. Dreiss; Y. Feng), Royal Society of Chemistry, Burlington House, Piccadilly (London) 2017.
- [18] a) D. Su, M. Yao, J. Liu, Y. Zhong, X. Chen, Z. Shao, ACS Appl. Mater. Interfaces. 2017, 9, 17489; b) X. Zhang, Z. Pan, Fibers Polym. 2022, 23, 2090.
- [19] J. Hong, Q. Lin, Z. Shao, ACS Macro Lett. 2023, 12, 888.
- [20] J. Sheng, W. Chen, K. Cui, L. Li, Rep. Prog. Phys. 2022, 85, 036601.
- [21] P. D. Olmsted, W. C. Poon, T. McLeish, N. Terrill, A. Ryan, Phys. Rev. Lett. 1998, 81, 373.
- [22] M. S. Zafar, D. J. Belton, B. Hanby, D. L. Kaplan, C. C. Perry, Biomacromolecules 2015, 16, 606.
- [23] a) Z. Zhu, Y. Kikuchi, K. Kojima, T. Tamura, N. Kuwabara, T. Nakamura, T. Asakura, J. Biomater. Sci., Polym. Ed. 2010, 21, 395; b) G. Fang, Y. Huang, Y. Tang, Z. Qi, J. Yao, Z. Shao, X. Chen, ACS Biomater. Sci. Eng. 2016, 2, 1992; c) J. Yan, G. Zhou, D. P. Knight, Z. Shao, X. Chen, Biomacromolecules 2010, 11, 1; d) Y. Yao, B. J. Allardyce, R. Rajkhowa, D. Hegh, S. Qin, K. A. S. Usman, P. Mota-Santiago, J. Zhang, P. Lynch, X. Wang, Macromol. Rapid Commun. 2022, 43, 2100891; e) M. Sun, Y. Zhang, Y. Zhao, H. Shao, X. Hu, J. Mater. Chem. 2012, 22, 18372.